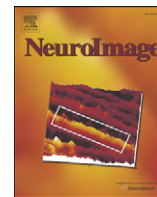




Contents lists available at ScienceDirect

NeuroImage

journal homepage: [www.elsevier.com/locate/ynimg](http://www.elsevier.com/locate/ynimg)



# Spatially sparse source cluster modeling by compressive neuromagnetic tomography

Wei-Tang Chang<sup>a</sup>, Aapo Nummenmaa<sup>b,c</sup>, Jen-Chuen Hsieh<sup>d,e</sup>, Fa-Hsuan Lin<sup>a,b,\*</sup>

<sup>a</sup> Institute of Biomedical Engineering, National Taiwan University, Taipei, Taiwan

<sup>b</sup> MGH-HST Athinoula A. Martinos Center for Biomedical Imaging, Charlestown, MA, USA

<sup>c</sup> Department of Biomedical Engineering and Computational Science, Aalto University School of Science and Technology, Espoo, Finland

<sup>d</sup> Institute of Neuroscience, National Yang-Ming University, Taipei, Taiwan

<sup>e</sup> Institute of Brain Science, National Yang-Ming University, Taipei, Taiwan

## ARTICLE INFO

### Article history:

Received 12 March 2010

Revised 1 May 2010

Accepted 6 May 2010

Available online 19 May 2010

### Keywords:

Inverse problem

$\ell^1$ -norm

convex optimization

MEG

EEG

Compressed sensing

Wavelet transform

## ABSTRACT

Magnetoencephalography enables non-invasive detection of weak cerebral magnetic fields by utilizing superconducting quantum interference devices (SQUIDS). Solving the MEG inverse problem requires reconstructing the locations and orientations of the underlying neuronal current sources based on the extracranial measurements. Most inverse problem solvers explicitly favor either spatially more focal or diffuse current source patterns. Naturally, in a situation where both focal and spatially extended sources are present, such reconstruction methods may yield inaccurate estimates. To address this problem, we propose a novel Compressive Neuromagnetic Tomography (CENT) method based on the assumption that the current sources are compressible. The compressibility is quantified by the joint sparsity of the source representation in the standard source space and in a transformed domain. The purpose of the transformation sparsity constraint is to incorporate local spatial structure adaptively by exploiting the natural redundancy of the source configurations in the transform domain. By combining these complementary constraints of standard and transformed domain sparsity we obtain source estimates, which are not only locally smooth and regular but also form globally separable clusters. In this work, we use the  $\ell^1$ -norm as a measure of sparsity and convex optimization to yield compressive estimates in a computationally tractable manner. We study the Laplacian matrix (CENT<sup>L</sup>) and spherical wavelets (CENT<sup>W</sup>) as alternatives for the transformation in the compression constraint. In addition to the two prior constraints on the sources, we control the discrepancy between the modeled and measured data by restricting the power of residual error below a specified value. The results show that both CENT<sup>L</sup> and CENT<sup>W</sup> are capable of producing robust spatially regular source estimates with high computational efficiency. For simulated sources of focal, diffuse, or combined types, the CENT method shows better accuracy on estimating the source locations and spatial extents than the minimum  $\ell^1$ -norm or minimum  $\ell^2$ -norm constrained inverse solutions. Different transformations yield different benefits: By utilizing CENT with the Laplacian matrix it is possible to suppress physiologically atypical activations extending across two opposite banks of a deep sulcus. With the spherical wavelet transform CENT can improve the detection of two nearby yet not directly connected sources. As demonstrated by simulations, CENT is capable of reflecting the spatial extent for both focal and spatially extended current sources. The analysis of *in vivo* MEG data by CENT produces less physiologically inconsistent “clutter” current sources in somatosensory and auditory MEG measurements. Overall, the CENT method is demonstrated to be a promising tool for adaptive modeling of distributed neuronal currents associated with cognitive tasks.

© 2010 Elsevier Inc. All rights reserved.

## Introduction

Magnetoencephalography (MEG) allows non-invasive detection of weak neuromagnetic fields with high temporal resolution by using superconducting quantum interference devices (SQUIDS) (Hamalainen

et al., 1993). The predominant physiological generators of both MEG and EEG signals are synchronous activations of cortical pyramidal cell populations (Hamalainen et al., 1993; Okada et al., 1997). Localization of the neural current sources is a crucial step in inferring the orchestration of regional cortical activity following experimental manipulation. Quantitative estimation of the strength, location, and orientation of the MEG and EEG source currents is tantamount to solving an electromagnetic inverse problem. Due to the ill-posed nature of this MEG/EEG inverse problem, the neuronal current reconstruction is not unique unless additional constraints are imposed (Helmholtz, 1853).

\* Corresponding author. Institute of Biomedical Engineering, National Taiwan University, Taipei, Taiwan.

E-mail address: [fhlin@nmr.mgh.harvard.edu](mailto:fhlin@nmr.mgh.harvard.edu) (F.-H. Lin).

Different types of constraints have been proposed for the MEG/EEG inverse problem, mainly motivated by computational tractability and/or physiological plausibility (Baillet et al., 2001; Hamalainen et al., 1993). Typically the constraints are formulated to explicitly favor spatially focal or diffuse source current distributions. The prior constraints can be combined with a MEG/EEG data fitting residual error measure to form a total cost function, which is then minimized to obtain the source estimates. The Minimum-Norm Estimate (MNE), which minimizes the  $\ell^2$ -norm of both the residual fitting error and the source distribution itself, can be obtained by using a closed-form linear inverse operator as the total cost function is quadratic (Hamalainen and Ilmoniemi, 1984). In probabilistic formulation, the MNE corresponds to an assumption that the *a priori* probability density function of the source current follows a Gaussian distribution with zero mean. Instead of minimizing the  $\ell^2$ -norm of the current estimates themselves, a method called LORETA favors spatially smooth current distributions, quantified by the  $\ell^2$ -norm of the first- or second-order spatial derivatives of the current sources (Pascual-Marqui et al., 1994). As a result of the minimum  $\ell^2$ -norm constraint, the spatial resolutions of MNE and LORETA (as measured by their point-spread functions) are relatively low.

Under some circumstances a useful interpretation of the MEG/EEG data requires spatially focal source representations. For example, Equivalent Current Dipole (ECD) fitting can be utilized to model the MEG/EEG data using a small number of point-like current dipoles by solving a nonlinear optimization problem, with either given or estimated dipole orientations and initial locations (Mosher et al., 1992). Because the cost function is not convex, the ECD fitting is computationally intensive as the number of dipoles increases. As another consequence of non-convexity, the ECD fitting can also be very sensitive to initial values assumed for the optimization algorithm (Mosher et al., 1992). Distributed source modeling can also provide spatially focal estimates by using the minimum  $\ell^1$ -norm as the prior cost function (Matsuura and Okabe, 1995), which is known as the minimum-current estimate (MCE) (Uutela et al., 1999). The noise sensitivity of  $\ell^1$ -norm solution can be reduced by applying singular value decomposition (SVD) on the forward solution matrix (Uutela et al., 1999) or on the selection of temporal basis functions from the measurement data (Ou et al., 2009). Nevertheless, the basic MCE is not suitable for modeling spatially extended current sources *per se*, since the minimum  $\ell^1$ -norm constraint penalizes such estimates.

Since the chosen distributed source model (e.g.,  $\ell^1$  vs.  $\ell^2$ ) directly produces bias toward either more focal or spatially extended currents estimates, it is difficult to select one particular source model without knowing *a priori* the possible spatial extents of the different sources. Considering a scenario in which both focal and distributed current sources are simultaneously present, minimizing the  $\ell^1$ -norm or the  $\ell^2$ -norm of the current distribution is not a desirable approach. To address this challenge, methods of automatically choosing an appropriate current model have been suggested. (Auranen et al., 2005) proposed a Bayesian analysis of the MEG inverse problem with  $\ell^p$ -norm priors, where  $p$  ( $1 \leq p \leq 2$ ) is considered unknown and determined from the data. However, the results show a general preference towards focal sources and *a priori* modeling of spatial correlations between source locations is not considered. The computational cost of the Markov Chain Monte Carlo sampling scheme is also relatively high.

Focal Vector field Reconstruction (FVR) provides another way to avoid preference toward focal or diffuse solutions, and it is closely related to our framework presented here. Unlike LORETA, which imposes the  $\ell^2$ -norm constraint of the first- or second-order spatial derivatives of the current sources alone, FVR promotes the sparsity of both the current distribution and its spatial derivatives (Haufe et al., 2008). However, the strict constraint of equality between the modeled data and regularized observed data can lead to noise-sensitivity of the solutions in low SNR conditions (see Discussion). Yet another strategy to tackle the problem of locally varying spatial source

extent is multi-resolution imaging, which considers submodels with low and high spatial resolutions to account for extended and compact neuronal currents, respectively (Cottereau et al., 2007). Such an approach generally requires high SNR in the measurements and is sensitive to errors in the forward solution (Limpiti et al., 2006).

The aim of the present study is to develop a distributed source modeling framework without exclusively assuming either focal or distributed current sources *a priori*. Instead of explicitly minimizing either the  $\ell^1$ - or the  $\ell^2$ -norm of current sources for a spatially sparse or diffuse solution, we hypothesize that the current sources are “compressible.” Here we use “compressible” to describe a digital image can be numerically represented by fewer coefficients corresponding to basis functions in a transformed domain. This hypothesis is motivated by several observations and theoretical considerations. First, natural images are mostly “compressible” as demonstrated by data compression studies (Taubman and Marcellin, 2002). The recently developed “compressed sensing” (CS) theory (Candes et al., 2006; Donoho, 2006) further exploits such redundancy to improve encoding and decoding efficiency in digital signal processing (Shannon, 1948). Using CS Magnetic Resonance Imaging (MRI) can achieve accelerated data acquisition beyond the limit of the Nyquist sampling theorem, provided that the image to be reconstructed is spatially sparse and compressible (Lustig et al., 2007). Second, the conventional hypothesis of distributed cortical processes being organized as mutual interactions between brain regions implies that spatially clustered neuronal activity should be expected also for MEG/EEG generators (Mesulam, 1990). Such spatial configurations are indeed numerically compressible and the compression of the current distributions can be effectively done with a suitable spatial transformation. The degree of compression is naturally related to the sparsity of the source current representation after the spatial basis transformation.

The sparsity of the estimates in the transformed domain, and thus the compressibility, can be achieved by minimizing the  $\ell^1$ -norm of the basis coefficients of the representation. Here we specifically focus on two compression transformations: second-order spatial derivatives (i.e., Laplacian matrix) and spherical wavelet transform (Schroder and Sweldens, 1995). Using individually collected MRI data for obtaining an anatomically realistic source space, we develop the ComprEssive Neuromagnetic Tomography (CENT) using the Laplacian matrix or the spherical wavelet transform on two-dimensional cortical surface manifold to estimate sources with compressive representations. The CENT method also incorporates the constraint of minimizing the  $\ell^1$ -norm of estimated current sources. This constraint promotes global spatial sparsity to generate separable clusters of activity, and reduces the excessive bias towards diffuse inverse estimates when using the Laplacian matrix or spherical wavelet transformation sparsity alone. When integrated, the dual sparsity constraint can be utilized to obtain a trade-off between spatially diffuse or focal sources. In addition, the discrepancy between the modeled and observed data is adaptively controlled to reduce the noise sensitivity of the solutions. As demonstrated by the simulations and somatosensory and auditory experiments, CENT provides improved accuracy for source reconstruction of MEG measurements involving both spatially focal and diffuse neuronal currents.

## Methods

### Forward model

The forward problem of MEG considers modeling the relationship between the measured signals and the underlying neuronal currents, which under the quasi-static Maxwell's equations is governed by a linear equation:

$$\mathbf{y}(t) = \mathbf{A}\mathbf{s}(t) + \mathbf{n}(t) \quad (1)$$

where  $\mathbf{y}(t)$  is an  $m$ -dimensional vector containing the observed MEG data from  $m$  sensors at time  $t$ ,  $\mathbf{A}$  is a  $m$ -by- $3n$  forward matrix,  $n$  is the number of points in the discretized source space,  $\mathbf{s}(t)$  is a  $3n$ -dimensional vector representing the unknown current source distribution with three Cartesian components at each source location, and  $\mathbf{n}(t)$  is measurement noise which is assumed additive and Gaussian. Usually  $3n$  is much larger than  $m$ , which renders the general form of the inverse problem severely underdetermined.

Each column of  $\mathbf{A}$  comprises of the signals in the MEG sensors that would be generated by a dipolar unit-strength current source element at a particular location, oriented along one of the coordinate axes in the source space. The calculation explicitly includes the primary current and volume current using a multicompartment conductivity model (Hamalainen et al., 1993). The conductance used in this study for brain, skull, and scalp compartments were 0.3 S/m, 0.06 S/m, and 0.3 S/m respectively. Specifically, we construct the forward matrix  $\mathbf{A}$  in such a way that a source location indexed by  $i$  is associated with three columns describing the MEG measurements from two locally tangential sources and one normal current source. The geometry is described with respect to the cortical surface derived from high resolution MRI data. Stacking up dipole components at all of the points in the source space, the instantaneous current dipole sources can be expressed as  $\mathbf{s}(t) = [\mathbf{s}_1(t)^T, \mathbf{s}_2(t)^T, \dots, \mathbf{s}_n(t)^T]^T$  with the following conventions: for each source space point  $i$ ,  $\mathbf{s}_i(t) = [s_{x,i}(t), s_{y,i}(t), s_{z,i}(t)]^T$ , the subscripts  $x$  and  $y$  indicate the two mutually orthogonal current sources tangential to the local cortical surface, and the subscript  $z$  indicates a current source oriented along the local outward normal of the cortical surface. Without loss of generality, we assume that Eq. (1) describes spatially whitened data such that the data vector, the forward matrix, and the noise vector have been multiplied by  $\mathbf{C}^{-1/2}$ , where  $\mathbf{C}$  is the estimated noise covariance matrix of the measurements and  $\mathbf{C}^{-1/2} = \mathbf{\Lambda}_C^{-1/2} \mathbf{U}_C^T$  is obtained from the eigenvalue decomposition  $\mathbf{C} = \mathbf{U}_C \mathbf{\Lambda}_C \mathbf{U}_C^T$ .

#### Compression transformation

Compressive Neuromagnetic Tomography (CENT) is based on the assumption of “compressible” current sources. The transformation part of the compression constraint is assumed to be linear, and consequently realizable as matrix multiplication on the ordinary current source space. In this article, we studied Laplacian matrix and spherical wavelet transform (Schroder and Sweldens, 1995) as possible linear compression transformations denoted in general by matrix  $\mathbf{M}$ . Employing Laplacian matrix in the cost function penalizes the spatial difference between the adjacent current sources on the cortical manifold. Using the spherical wavelet transform in the cost function penalizes the spatial difference between the vertices in the Butterfly wavelet basis (see Fig. 2). For this case, the spatial difference

between the current sources is penalized roughly in inverse proportion to their surface distance (Schroder and Sweldens, 1995).

In practice, it is necessary to derive a semi-regular multi-resolution cortical model (Wood et al., 2000) from a 2D anatomical cortical model in order to implement the compression transformation explicitly. The procedure of constructing such a multi-resolution cortical model is illustrated in Fig. 1. The first step is to morph each of the inflated cortical hemisphere surfaces onto a spherical coordinate system (Dale et al., 1999). The multi-level representation of the cortical surface is accomplished by recursively dividing each of the triangular faces on the spherical surface into four smaller triangles. Finally, the multi-level representation is transformed back to individual's anatomical space. Given the semi-regular multi-resolution cortical model, we can calculate either the Laplacian matrix or spherical wavelet transform in a straightforward manner.

#### Laplacian matrix

From a physiological point of view, neighboring neural populations are more likely to be active synchronously (Engel et al., 1990; Silva et al., 1991). This physiological constraint can be incorporated into the inverse estimation by applying the Laplacian matrix (Bradshaw and Wikswo, 2001) on the cortical surfaces. The Laplacian matrix comprises of the second-order spatial derivatives:

$$M_{uv}^L = \begin{cases} 1, & u = v \\ -\frac{1}{\sqrt{d_u d_v}}, & (u, v) \in \mathbf{E} \\ 0, & \text{otherwise} \end{cases} \quad (2)$$

where  $M_{uv}^L$  denotes the element at the  $u$ th row and  $v$ th column in the  $n$ -by- $n$  matrix  $\mathbf{M}^L$ ,  $d_i$  denotes the number of immediate neighbors of current source  $i$ , and  $\mathbf{E}$  denotes the set of edges of the triangulated cortical model.

#### Spherical wavelet transform

Wavelets have been proven to be powerful bases for signal compression. The implementation of spherical wavelet transform on cortical manifolds is based on the lifted Butterfly bases (Schroder and Sweldens, 1995) and the wavelet coefficients can be naturally computed using a lifting scheme. The reason of employing Butterfly bases is that Butterfly can more parsimoniously represent the signal at a specified error (Schroder and Sweldens, 1995). The vertices in a Butterfly basis are shown in Fig. 2. The same lattice structure is used in different spatial scales of the semi-regular multi-resolution cortical model. In contrast to the Laplacian matrix, vertices utilized in a

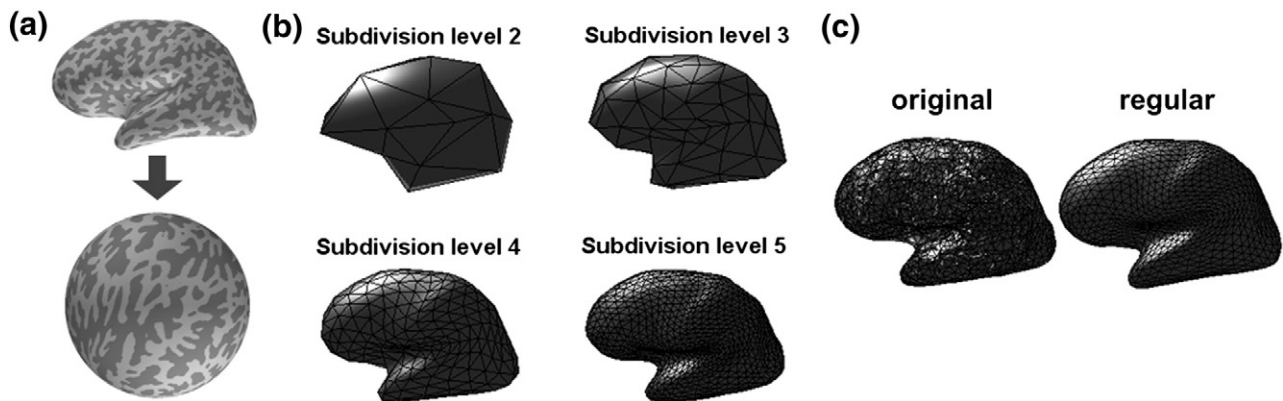


**Fig. 1.** The procedure of generating semi-regular multi-resolution mesh. (a) Morphing the inflated cortical surface into a unit sphere. (b) Recursively subdividing the unit sphere and morphing the sphere back into the original inflated cortical surface. (c) Comparing between the original cortical mesh and the semi-regular cortical mesh.

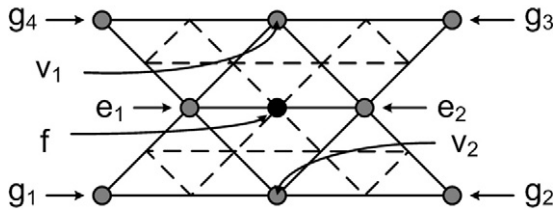


**Fig. 2.** The vertices in Butterfly bases.  $f$  is the vertex in the finer resolution level.  $e_1, e_2, v_1, v_2, g_1, g_2, g_3$  and  $g_4$  are the members of the neighbors used in the bases.

Butterfly basis are located in the vicinity of a given point but they are not nearest neighbors. The whole spherical wavelet transform can be written as one extremely large-scale sparse matrix multiplication to facilitate solving of a convex optimization problem.

#### Compressive Neuromagnetic Tomography: cost function and optimization

Since the CENT method relies on large-scale convex optimization techniques, the computational efficiency can be improved by reducing the sizes of the variables with only a slight loss of information. Let  $\mathbf{A}_r$  denote the forward matrix with a reduced rank, obtained by using the truncated singular value decomposition (tSVD):  $\mathbf{A} = \mathbf{U}\mathbf{\Lambda}\mathbf{V}^T$  and  $\mathbf{A}_r = \mathbf{U}_r^T\mathbf{A} = \mathbf{\Lambda}_r\mathbf{V}_r^T$ , where  $\mathbf{U}_r$  and  $\mathbf{V}_r$  are the left and right singular vector matrices constructed from the first  $r$  columns of  $\mathbf{U}$  and  $\mathbf{V}$ , respectively. By definition,  $\mathbf{\Lambda}_r$  is a  $r$ -by- $r$  diagonal matrix with the first  $r$  diagonal elements of  $\mathbf{\Lambda}$ . In addition to improving the computational efficiency, using the truncated forward matrix  $\mathbf{A}_r$  reduces the noise sensitivity of  $\ell^1$ -type estimates (Huang et al., 2006; Uutela et al., 1999). We also perform the corresponding orthogonal transformation on the measurements:  $\mathbf{y}_r(t) = \mathbf{U}_r^T\mathbf{y}(t)$ . In this study, we chose the truncation index  $r$  so that we retain 99% of the total lead field power (Lin et al., 2006).

To construct the CENT cost function, we presume that the efficiency of the source compression can be reasonably quantified by the integrated  $\ell^1$ -norm of the sources in the standard and transformed domains (see Appendix A for details). We choose the  $\ell^1$ -norm cost in order to implement the prior assumption that the “compressed” source representation should have a sparse nature. The CENT can be mathematically described as constrained minimization of a cost function:

$$\min_{\mathbf{s}(t)} \|\mathbf{M}\mathbf{s}^{\ell^2}(t)\|_1 + \alpha\|\mathbf{s}^{\ell^2}(t)\|_1 \text{ s.t. } \|\mathbf{y}_r(t) - \mathbf{A}_r\mathbf{s}(t)\|_2^2 < \varepsilon, \quad (3)$$

where  $\mathbf{M}$  is the compression transformation matrix. The  $\mathbf{s}^{\ell^2}(t)$  denotes a vector consisting of the local  $\ell^2$ -norms of orientation weighted dipole moments  $[s_1^{\ell^2}(t), s_2^{\ell^2}(t), \dots, s_n^{\ell^2}(t)]^T$ , where the local  $\ell^2$ -norm  $s_i^{\ell^2}(t)$  ( $1 \leq i \leq n$ ) at the  $i$ th source location is defined as:

$$\mathbf{s}_i^{\ell^2}(t) = \left\| [w_{x,i}s_{x,i}(t), w_{y,i}s_{y,i}(t), w_{z,i}s_{z,i}(t)]^T \right\|_2. \quad (4)$$

The coefficients  $[w_{x,i}, w_{y,i}, w_{z,i}] = [1/\sin \theta_i, 1/\sin \theta_i, 1]$  are the orientation weights for  $s_{x,i}(t)$ ,  $s_{y,i}(t)$ , and  $s_{z,i}(t)$  at the  $i$ th current source location respectively,  $\theta_i$  can take any value between  $0^\circ$  and  $90^\circ$  in order to impose a more or less flexible constraint on the orientation of current sources. Note that a small  $\theta_i$  is likely to render the estimated current source at location  $i$  predominantly oriented perpendicular to the local cortical surface. The value of the parameter  $\theta_i$  in this work was globally set to  $30^\circ$  (Lin et al., 2006). In fact,  $\theta_i$  can be also individually tuned in order to account for the variation of source orientations (Lin et al., 2006). The parameter

$\alpha$  in Eq. (3) determines the relative importance of the *a priori* cost function terms, a higher value of  $\alpha$  favoring more focal solutions. The parameter  $\alpha$  can be appropriately fixed based on simulations (see Results section).

Let us now consider the data fit residual constraint, and let  $\varepsilon$  be the specified residual variance controlling the consistency between the observed data and the data modeled by using the source estimates. It has been suggested that a suitable  $\varepsilon$  can be chosen by requiring that the probability of  $\|\mathbf{y}_r(t) - \mathbf{A}_r\mathbf{s}(t)\|_2^2 \geq \varepsilon$  is reasonably small (Ding and He, 2008). Using the whitened measurements and assuming that each MEG sensor is contaminated by Gaussian white noise with variance  $\sigma^2$ , we have  $\|\mathbf{y}_r(t) - \mathbf{A}_r\mathbf{s}(t)\|_2^2 / \sigma^2 \sim \chi_r^2$ , where  $\chi_r^2$  is the Chi-square distribution with  $r$  degrees of freedom. In practice, after whitening  $\sigma^2 = 1$ . Thus the parameter  $\varepsilon$  can be selected so that the probability of  $\|\mathbf{y}_r(t) - \mathbf{A}_r\mathbf{s}(t)\|_2^2$  integrated over the interval  $[0, \varepsilon]$  is high (e.g., 0.99). With this additional condition, Eq. (3) can be solved by convex optimization techniques (Grant and Boyd, 2009).

In summary, we propose CENT<sup>L</sup> and CENT<sup>W</sup> using Laplacian  $\mathbf{M}^L$  and spherical wavelet transformation  $\mathbf{M}^W$  as the compression matrix respectively:

$$\begin{aligned} \text{CENT}^L &\equiv \arg \min_{\mathbf{s}(t)} \|\mathbf{M}^L\mathbf{s}^{\ell^2}(t)\|_1 + \alpha\|\mathbf{s}^{\ell^2}(t)\|_1 \text{ s.t. } \|\mathbf{y}_r(t) - \mathbf{A}_r\mathbf{s}(t)\|_2^2 < \varepsilon, \text{ or} \\ \text{CENT}^W &\equiv \arg \min_{\mathbf{s}(t)} \|\mathbf{M}^W\mathbf{s}^{\ell^2}(t)\|_1 + \alpha\|\mathbf{s}^{\ell^2}(t)\|_1 \text{ s.t. } \|\mathbf{y}_r(t) - \mathbf{A}_r\mathbf{s}(t)\|_2^2 < \varepsilon. \end{aligned} \quad (5)$$

Both estimates CENT<sup>L</sup> and CENT<sup>W</sup> have the characteristics of being globally focal and locally smooth. However, CENT<sup>W</sup> can separate spatially close but not directly connected clusters of current sources better than CENT<sup>L</sup>, as demonstrated in later sections. As mentioned before, the inverse problem in this case is formally a convex optimization problem since  $\ell^1$ -norm and  $\ell^2$ -norm are convex functions (Boyd, 2004). For implementation we used CVX, a software package for specifying and solving convex problems (Grant and Boyd, 2009). Specifically, we used the following convex formulation of the optimization problem to solve Eq. (5):

$$\langle \hat{\mathbf{s}}, \hat{\mathbf{s}}^{\ell^2}, \hat{q}, \hat{z} \rangle = \arg \min_{\mathbf{s}, \mathbf{s}^{\ell^2}, q, z} (q + \alpha z) \quad (6)$$

$$\text{s.t. } \|\mathbf{y}_r - \mathbf{A}_r\mathbf{s}\|_2^2 < \varepsilon, \text{ with}$$

$$\left\| [w_{x,i}s_{x,i}, w_{y,i}s_{y,i}, w_{z,i}s_{z,i}]^T \right\|_2 \leq s_i^{\ell^2}, \forall i = 1, \dots, n,$$

$$\|\mathbf{M}\mathbf{s}^{\ell^2}\|_1 \leq q, \text{ and } \|\mathbf{s}^{\ell^2}\|_1 \leq z.$$

Auxiliary variables  $q$  and  $z$  are introduced to convert the  $\ell^1$  cost function into a standard convex optimization form by augmenting the problem with additional constraints. When the solutions are at the minimum, these inequality constraints in Eq. (6) are satisfied with equality, and the cost is reduced to the  $\ell^1$ -norm. Otherwise, the cost function can be further reduced.

#### Performance measures

In simulations, performances of the MEG inverse solution methods were assessed with the following three metrics: (1) spatial dispersion (SD), which measures how source locations are spatially blurred, (Molins et al., 2008) (2) distance of localization error (DLE), which measures the averaged error distance between the true source locations and the maximum of source estimates (Molins et al., 2008),



and (3) receiver operating characteristic (ROC) curve, which quantifies the detection power (Van Trees, 1968). In the following, each individual source in a distributed source configuration (i.e., an extended cortical patch) is considered a “true source”.

The SD is defined as:

$$SD = \sqrt{\frac{\sum_{k=1}^K \sum_{i \in I_k} d_{ki}^2 \|\hat{\mathbf{s}}_i\|_2^2}{\sum_{i=1}^n \|\hat{\mathbf{s}}_i\|_2^2}}, I_k = \left\{ i \mid k = \arg \min_{k'} \{d_{k'i}\} \right\}, 1 \leq k \leq K, 1 \leq k' \leq K, \quad (7)$$

where  $d_{ki}$  denotes the distance between the  $k$ th true source and the  $i$ th source estimate, and  $K$  is the number of the underlying current sources.  $I_k$  is the set of source space indices for which the  $k$ th of true sources is the spatially closest. To avoid overriding contributions from source estimates with small values but large distances, as present typically for instance in the MNE, only source estimates with magnitude exceeding 10% of the global maximum were taken into the calculation of  $I_k$ .

The DLE is defined as

$$DLE = \frac{1}{K_J} \sum_{k \in J} DLE_k, J = \{k \mid I_k \neq \emptyset\}, \quad (8)$$

$$DLE_k = \left\{ d_{ki} \mid i = \arg \max_{i'} (\|\hat{\mathbf{s}}_{i'}\|_2), i' \in I_k \right\},$$

where  $K_J$  denotes the number of elements in  $J$ , which is the set including indices of the detected true sources. The  $DLE_k$  measures the distance between the  $k$ th true source and maximum source estimate in  $I_k$  and DLE is the average of  $DLE_k$  over the true source indices  $k$ .

The ROC curve is a graphical plot of the probability of false positive detection (FP) vs. probability of true positive detection (TP) as the discrimination threshold varies. The probability of missing true current sources is (1-TP). We measure the area under an ROC curve to quantify the detection power: minimal and maximal detection powers have areas of 0.5 and 1, respectively (Van Trees, 1968). The FP and the (1-TP) required for an ROC curve are defined as

$$1 - TP = 1 - \frac{N_d}{N_s} \text{ and } FP = \frac{N_{fd}}{n - N_s}, \quad (9)$$

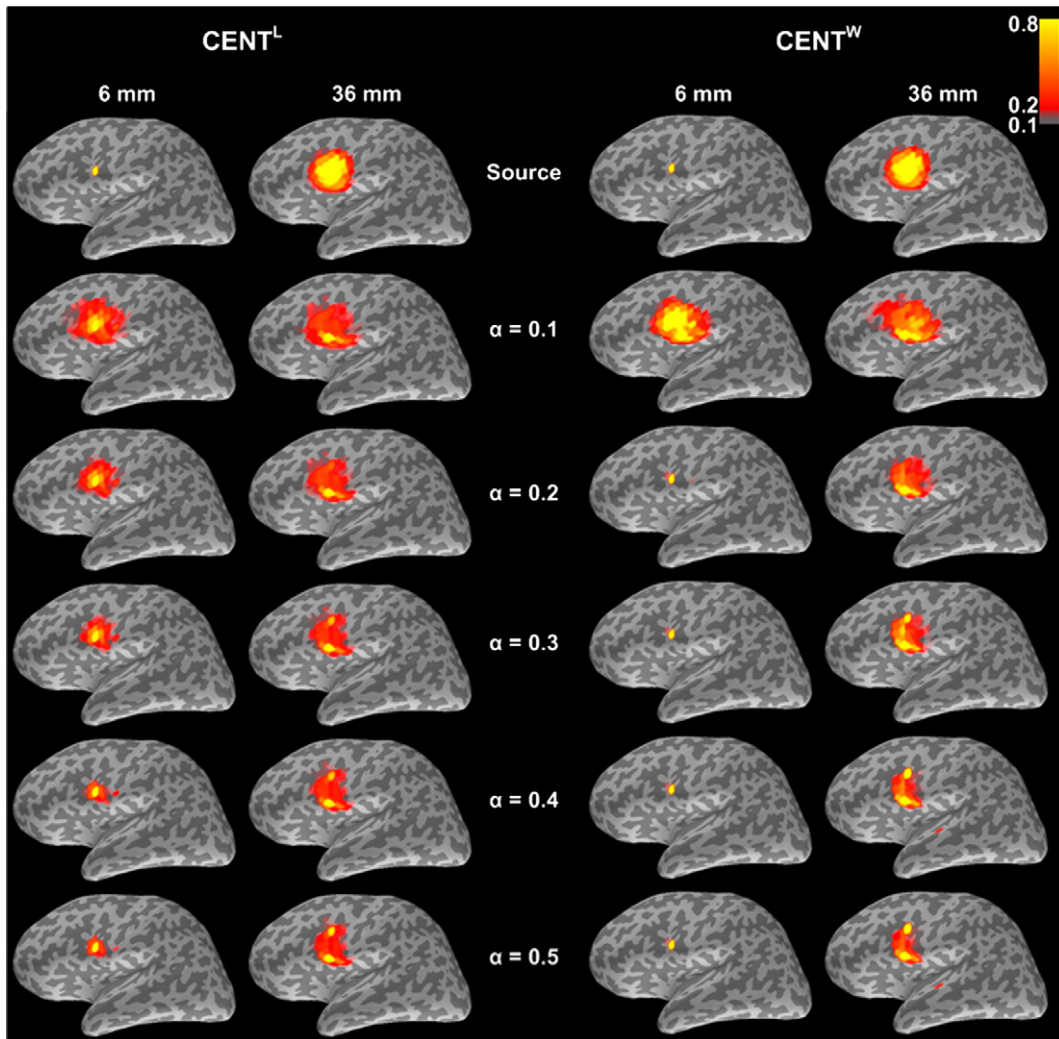


**Fig. 3.** Linearly scaled reconstructions between 1.0 and 0.0 obtained using  $\mathbf{M}^L$  (left side) and  $\mathbf{M}^W$  (right side) as the compression matrix. The simulated current sources shown in the top row are located at the inferior frontal gyrus and have spatially Gaussian distributions. The FWHMs of the two different source configurations are 6 mm and 36 mm. The corresponding source estimates with  $\alpha$  varying between 0.1 and 0.5 are shown from the second to the bottom row, individually. The color-coded source estimates are rendered on the inflated left hemisphere cortical surface.

where  $N_d$  and  $N_{fd}$  are numbers of detected true and false sources, respectively. The number of total estimated sources at a given threshold is  $N_d + N_{fd}$  and the number of true sources is  $N_s$ .

## Materials

### Anatomical information from high resolution MRI

Structural MRI data were acquired on a 3T MRI scanner (Tim Trio, SIEMENS Medical Solutions, Erlangen, Germany) using a T1-weighted 3D MPRAGE sequence with following parameters: repetition time/echo time/inversion time [TR/TE/TI] = 2,530/3.49/1,100 ms, flip angle = 7 degree, partition thickness = 1.33 mm, image matrix =  $256 \times 256$ , 128 partitions, and a field-of-view =  $21 \text{ cm} \times 21 \text{ cm}$ . Because the most significant sources of MEG signals are postsynaptic currents in the pyramidal cells on the cortex (Okada et al., 1997), the locations of these sources can be constrained to the cortical mantle (Dale and Sereno, 1993). We used the FreeSurfer software (Dale et al., 1999; Fischl et al., 1999) to perform segmentation and to build cortical surface meshes from the MRI data. These cortical surfaces were used for 1) generating the source space in MEG sources analysis, 2) calculating the forward solution  $\mathbf{A}$  with realistic anatomy, and 3) rendering the source localization result. The constrained source space was defined on the cortical surface as the boundary between the gray and white matter. FreeSurfer generated triangulated surface models with 130,000–150,000 vertices per hemisphere (each vertex was approximately separated by 1 mm). Due to the limited nature of information on the sources provided by the 306 channels of extracranial MEG measurements, we created a semi-regular multi-resolution cortical model with 1026 dipole locations in each hemisphere, where the average distance

between any two neighboring source dipoles was 10 mm. The co-registration between MEG and MRI coordinates was done by manually registering three fiducial points between the MEG data and the MPRAGE data. The MEG forward solution was calculated using a single layer boundary element model (BEM) (Hamalainen and Sarvas, 1989; Oostendorp and van Oosterom, 1989) based on the inner-skull surface created by the FreeSurfer.

### Simulated MEG data

To simulate MEG data, we created clusters of current dipoles on the cortical surface. Unless otherwise specified, the simulation current source orientations in this study were adjusted to be perpendicular to the local cortical surface informed by the high resolution MRI data. Simulated ideal MEG data were generated from the product between the forward matrix  $\mathbf{A}$  and a vector of the current sources  $\mathbf{s}(t)$ . Gaussian white noises were added to the simulated ideal MEG data. The SNR was defined as  $\frac{\|\mathbf{A}\mathbf{s}(t)\|_2}{m}$ . To examine the statistical behavior of the inverse techniques and its noise sensitivity, we repetitively estimated the current sources for 100 realizations of the noise at each specified SNR.

In one simulation condition, either a focal (source extent full-width half-magnitude (FWHM) of 6 mm) or a diffuse (source extent FWHM of 36 mm) current source was placed at the left inferior frontal gyrus, as shown in the top row of Fig. 3. In the other simulation condition, we had all pair-wise combinations of a focal and a diffuse source at the inferior frontal gyrus (IFG) and the middle temporal gyrus (MTG), respectively (the top row of Fig. 4). These source configurations were designed to test whether our method can provide satisfactory source estimates from MEG measurements arising from different combinations of compact and extended sources.

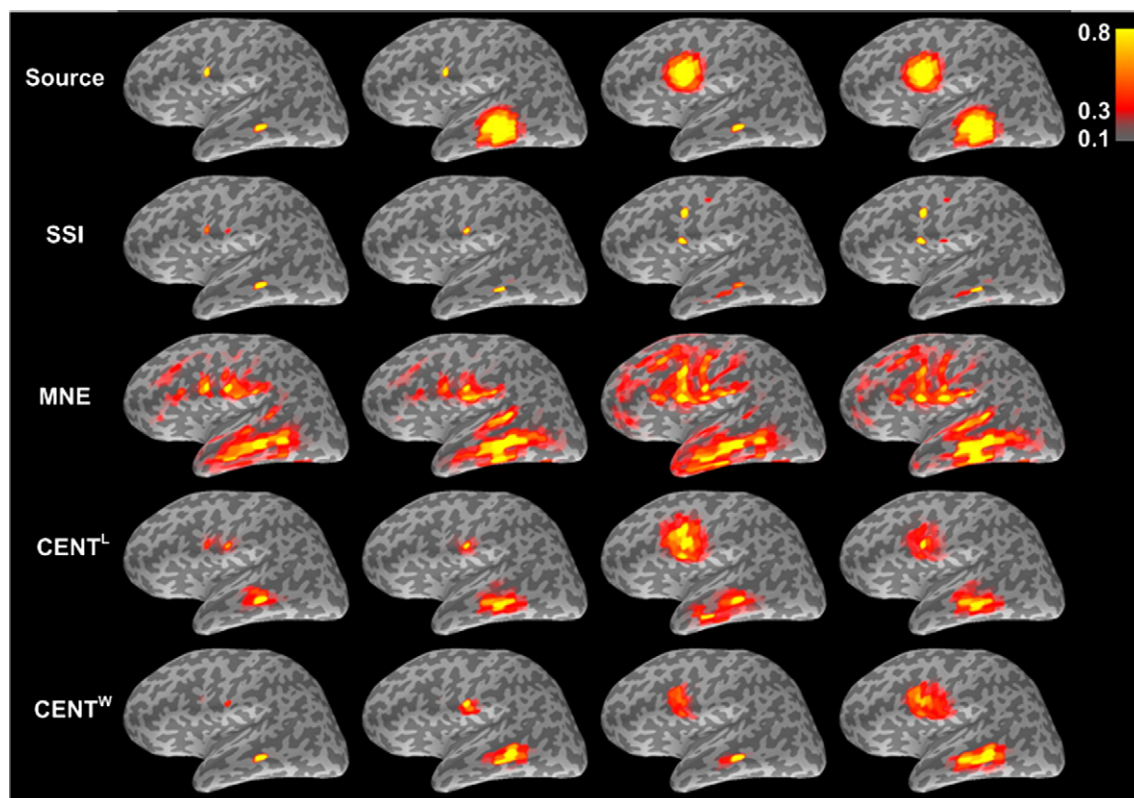


**Fig. 4.** Cortical maps of different source configurations and the corresponding localization results using different methods. All pair-wise combinations between focal and diffuse sources were studied. From the second to the bottom rows are the source reconstructions using SSI, MNE,  $\text{CENT}^L$ , and  $\text{CENT}^W$ . The activation strength is color-coded as illustrated by the color bar.

## MEG experiments

To test the method with empirical data, we performed somatosensory and auditory MEG experiments. The experiments were conducted with six healthy, right-handed subjects (4 males, 2 females; average age = 27 years) with the approval of the institutional review board (IRB) of our institutes. Prior to the experiments, an informed consent was obtained from each subject. A 306-channel MEG system (Vector-View, Elekta-Neuromag Oy, Helsinki, Finland) was used to record the neuromagnetic responses.

In the somatosensory study, the right median nerve was stimulated at the wrist with current pulses of 0.2 ms duration (Konstant-Strom Stimulator, Lucius & Baer, Geretsried, Germany). The amplitude of the stimulation was adjusted to clearly observe thumb adduction. The inter-stimuli-interval between the pulses was 5 seconds. We collected 180 trials in total. In the auditory experiment, 1 kHz pure tone stimuli were presented to the right ear. The inter-stimulus-interval between the stimuli was 4 seconds. About 100 responses were averaged. The measurement bandwidth was 0.03 Hz to 260 Hz and the data were digitized at 1004 Hz.

## Implementation

A semi-regular multi-resolution cortical model was calculated from the 'Toolbox Wavelets on Meshes' (Peyre, 2008). To perform convex optimization, we employed the CVX software package (Grant and Boyd,

2009). Both toolboxes run in MATLAB (Mathworks, Natick, MA). The convex optimization converged within 100 iterations in all of our simulations and experimental data conditions. For  $n=2052$  and  $m=306$ , our current implementation takes about 30 s per sampled time point with a standard PC (1.6 GHz CPU and 2 Gbytes RAM). The computation can be further accelerated by parallel implementations (Nakata et al., 2006) but these aspects go beyond the scope of this study. For visualization, all source estimates in the simulation were linearly scaled between 1 and 0.

## Results

### Simulations

We first investigate the sensitivity of  $CENT^L$  and  $CENT^W$  to the parameter  $\alpha$ . A large  $\alpha$  leads to a relatively focal and small  $\alpha$  to a more smooth solution. Using simulated data with infinite SNR, we found that  $\alpha=0.1\sim 1$  entails a reasonable balance between  $\|s^{(2)}(t)\|_1$  and  $\|Ms^{(2)}(t)\|_1$ . Maps of source estimates are shown in Fig. 3, respectively. We found that  $\alpha=0.4$  can successfully detect either focal (a 6 mm FWHM cortical patch) or diffuse (a 36-mm FWHM cortical patch) sources in  $CENT^L$  and  $CENT^W$ . In this paper, we chose  $\alpha=0.4$  for the rest of simulations.

In Fig. 4, we show the comparison between  $CENT^L$ ,  $CENT^W$ , previously reported sparse source imaging (SSI) approach (Ding and He, 2008), where  $\mathbf{M}$  is an identity matrix, and the MNE. The simulated

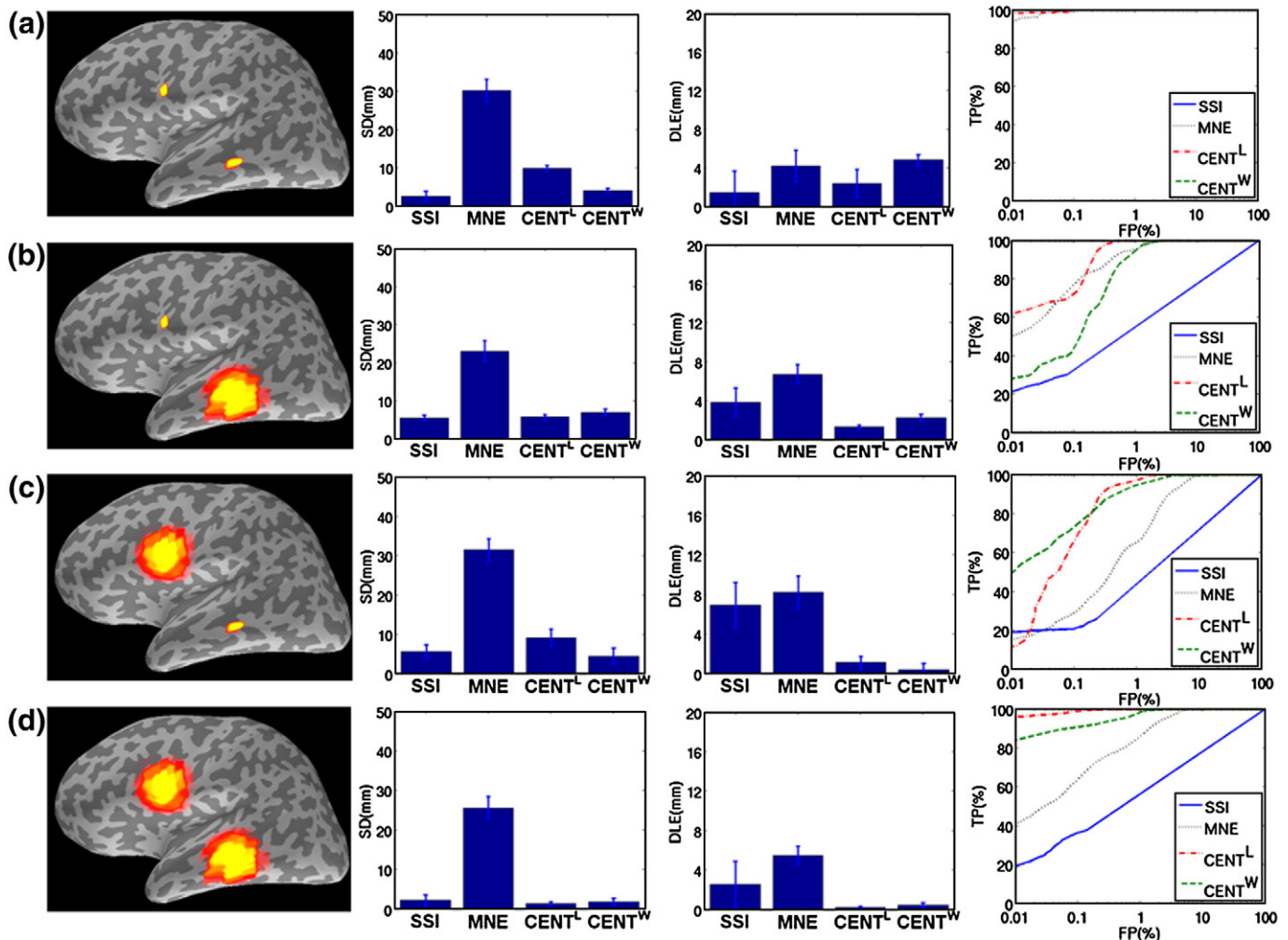


Fig. 5. The simulated sources (left column), SD (middle left column), DLE (middle right column) and ROC (right column) metrics on the reconstructed sources. Note that the x axes of the ROC metric are in log-scale.



**Table 1**

The areas under the ROC curves in Fig. 5. An area of 1 represents a perfect detection; an area of 0.5 reflects essentially no detection.

Source configuration	SSI	MNE	CENT <sup>L</sup>	CENT <sup>W</sup>
Fig. 5a	IFG: focal	1.0000	1.0000	1.0000
Fig. 5b	MTG: focal	1.0000	1.0000	1.0000
Fig. 5b	IFG: focal	0.6497	0.9985	0.9995
Fig. 5c	MTG: diffuse	0.6497	0.9985	0.9979
Fig. 5c	IFG: diffuse	0.6292	0.9879	0.9987
Fig. 5d	MTG: focal	0.6292	0.9879	0.9984
Fig. 5d	IFG: diffuse	0.6871	0.9957	1.0000
Fig. 5d	MTG: diffuse	0.6871	0.9957	0.9996

MEG current sources are displayed in the top row in Fig. 4. The SSI generates globally focal source estimates regardless of the underlying source configurations due to the nature of the  $\ell^1$ -norm constraint on the estimated source strengths. On the other hand, MNE produces overly diffuse source estimates because of the  $\ell^2$ -norm constraint. The source estimates of CENT<sup>L</sup> and CENT<sup>W</sup> can flexibly and more accurately reflect the spatial extent of the true simulated sources in the four separate simulations. When both simulated sources were focal, both CENT<sup>L</sup> and CENT<sup>W</sup> estimated focal sources (Fig. 4; left column). For the case of two diffuse simulated sources, CENT<sup>L</sup> and CENT<sup>W</sup> both estimated spatially extended sources (Fig. 4; right column). Note that CENT<sup>W</sup> can provide a spatially more clear distinction between the simulated focal and diffuse source pairs than CENT<sup>L</sup>. For the combination of compact and extended sources, CENT<sup>L</sup> and CENT<sup>W</sup> are both more similar to the underlying sources than SSI and MNE.

The above simulations were further quantified and results are shown in Fig. 5. SSI generated sparse solutions and therefore demonstrated a low SD. However, SSI solutions show inferior performance than CENT<sup>L</sup> and CENT<sup>W</sup> in DLE and ROC for the extended sources. The SD and DLE of MNE are always larger than SSI, CENT<sup>L</sup> and CENT<sup>W</sup>. Quantified by the SD metric, the spatial resolution of CENT<sup>L</sup>, CENT<sup>W</sup> and SSI are similar. However, source localization accuracy of both CENT<sup>L</sup> and CENT<sup>W</sup> is higher than SSI by showing a smaller DLE metric. All the differences of SD and DLE between SSI/MNE and CENT<sup>L</sup>/CENT<sup>W</sup> were statistically significant ( $p < 0.05$ ) in a paired t-test. In the ROC analysis, the detection sensitivity is measured by the area under the ROC curve, where a larger area implies higher detection sensitivity. As presented in Table 1, CENT<sup>L</sup> outperforms SSI and MNE whenever there is one or more spatially diffuse sources. Even with focal sources only (the top row of Fig. 5), both CENT<sup>L</sup> and CENT<sup>W</sup> have detection sensitivity similar to that of SSI. In general, CENT<sup>L</sup> and CENT<sup>W</sup> demonstrate quantitatively and qualitatively the benefit of using the compressibility constraint in the source reconstruction.

Since the MEG field patterns are similar for sources across a sulcus, it is quite common to obtain source estimates on both banks of the

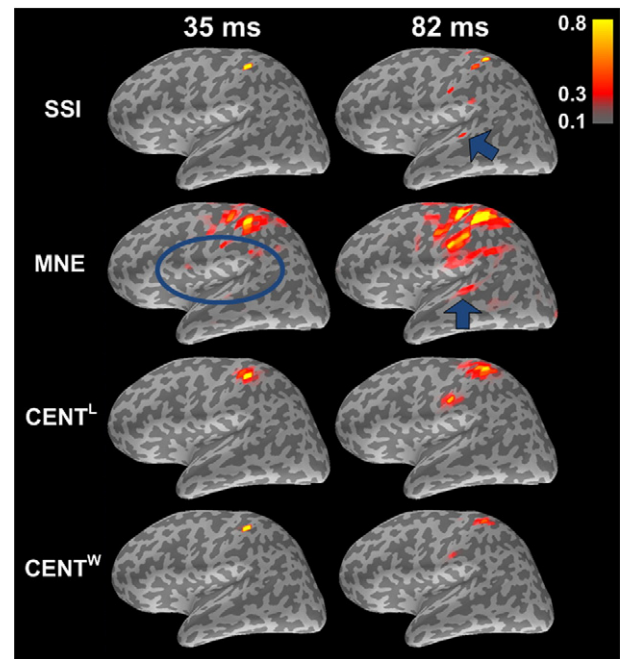


**Fig. 7.** Maps of source estimates in a somatosensory MEG experiment. From left to right are presented the activation maps at 35 and 82 ms after stimulus onset. The source estimates of SSI, MNE, CENT<sup>L</sup> and CENT<sup>W</sup> are listed from top to bottom. The source strength has been linearly scaled between 1 and 0 and is color-coded as illustrated by the color bar. The blue arrows and the blue ellipsoid indicate the potentially spurious source locations.

sulcus even when true current source is located only on one side. It is also highly difficult to discern two distributed sources as separate activations, when they are spatially adjacent to each other. These two difficult localization conditions were further investigated in the following two cases. In the first case, a group of simulated current dipoles was located at left secondary somatosensory area (SII) (Fig. 6). As the results shown in Case 1 in Fig. 6, MNE, CENT<sup>L</sup> and CENT<sup>W</sup> correctly estimated the source at left SII, while SSI detected only part of the source. However, MNE also reported strong source on the superior temporal gyrus (STG; indicated by a blue arrow in Fig. 6), which is anatomically adjacent to the SII area in the folded cortical surface. Compared to MNE, CENT<sup>W</sup> reported relatively weak source on left STG but not as weak as CENT<sup>L</sup>. The constraint of spatial smoothness of the Laplacian matrix encouraged sources estimates of immediate neighbors in CENT<sup>L</sup>, which consequently makes this method less prone to producing source estimates on the wrong side of the fissure. In case 2, we generated two separate but spatially close

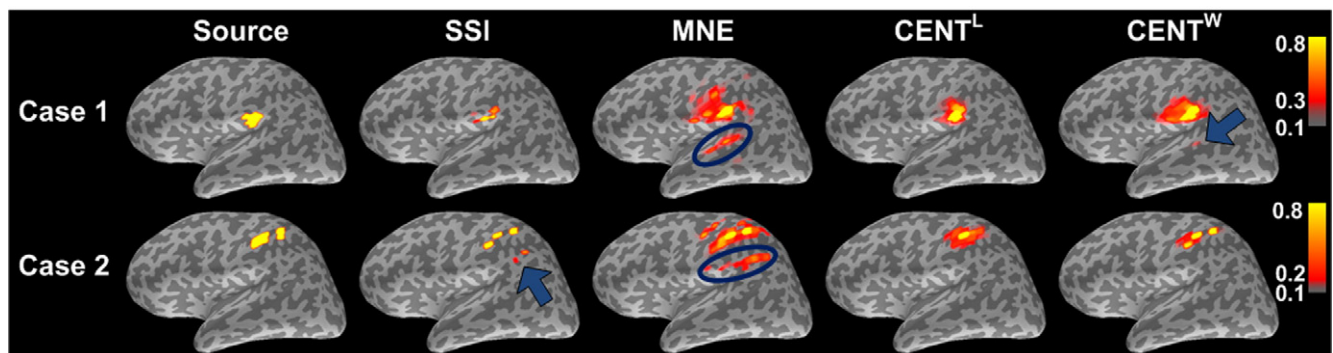


**Fig. 6.** Reconstructions of SSI, MNE, CENT<sup>L</sup> and CENT<sup>W</sup> using two different source configurations. The left-most column represents the simulated sources. Reconstructed signals of SSI, MNE, CENT<sup>L</sup> and CENT<sup>W</sup> are followed from left to right. The activation strength is linearly scaled between 1 and 0 and is color-coded as illustrated by the color bar. The blue arrows and the blue ellipsoids indicate the false positives.



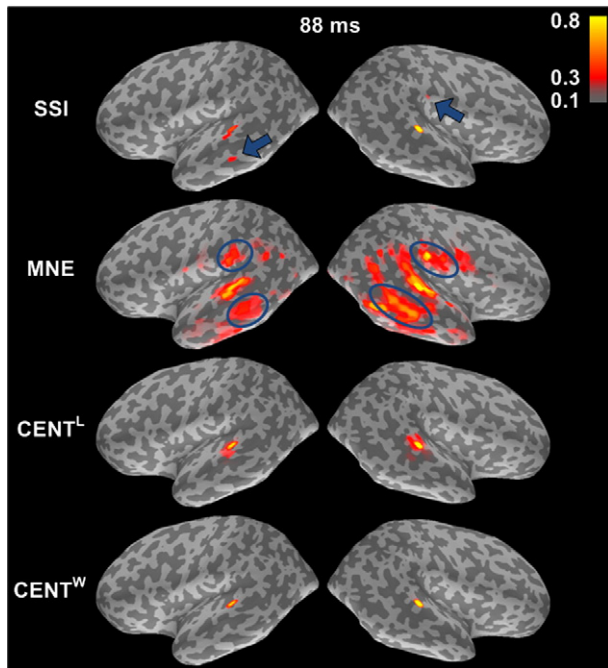


**Fig. 8.** Maps of source estimates in an auditory MEG experiment. All of the maps are snapshots at 88 ms after the stimulus onset. The source estimates of SSI, MNE,  $CENT^L$  and  $CENT^W$  are listed from top to bottom. The source strength has been linearly scaled between 1 and 0 and is color-coded as illustrated by the color bar. The blue arrows and ellipsoids indicate the potentially spurious source locations.

sources on the post-central gyrus in order to test the ability of SSI, MNE,  $CENT^L$  and  $CENT^W$  on distinguishing these two sources. In Fig. 6,  $CENT^W$  demonstrates best separation of two sources than MNE and

$CENT^L$ . Although SSI also demonstrated separate sources on the post-central gyrus due to the sparse nature of  $\ell^1$ -norm solution, SSI reported false positives on the supramarginal gyrus. Since vertices in the wavelet basis vectors are not necessarily immediate neighbors, some spatial discontinuity is allowed and less penalized in  $CENT^W$  than in  $CENT^L$ .

#### Somatosensory and auditory MEG experiments

We also applied the CENT methodology to the evoked somatosensory and auditory MEG data. It has been shown that the median-nerve stimulus can activate a complex cortical network (Hari and Forss, 1999) including the primary somatosensory cortex (SI) contralateral to the stimulus and the bilateral secondary somatosensory cortices (SII). The SI cortical area typically shows the first peak occurring at around 20 ms after the median nerve stimulation, followed by the next deflection at around 35 ms, which might reflect polysynaptic input or cortical inhibition. SII responses were found bilaterally, and as usual the contralateral side shows stronger activation, with the peak around 100 ms after stimulation.

In Fig. 7, we show the source estimates using SSI, MNE,  $CENT^L$  and  $CENT^W$  in the right median nerve stimulation MEG experiment. Blue arrows indicate the potentially spurious source locations, which are not reported in the literature. At 35 ms, all methods estimated the left SI sources on the posterior wall of the central sulcus. The MNE, however, estimated sources also at the left SII area, which is physiologically less likely at this early timing. At 82 ms, all the methods estimated activations at the left SII. In addition, SSI and MNE also reported current sources at the superior temporal gyrus. These sources are considered less likely to be present in the median nerve stimulation experiment.

For the auditory experiment, Fig. 8 shows the SSI, MNE,  $CENT^L$  and  $CENT^W$  at 88 ms after the stimulus onset. Previous studies have shown

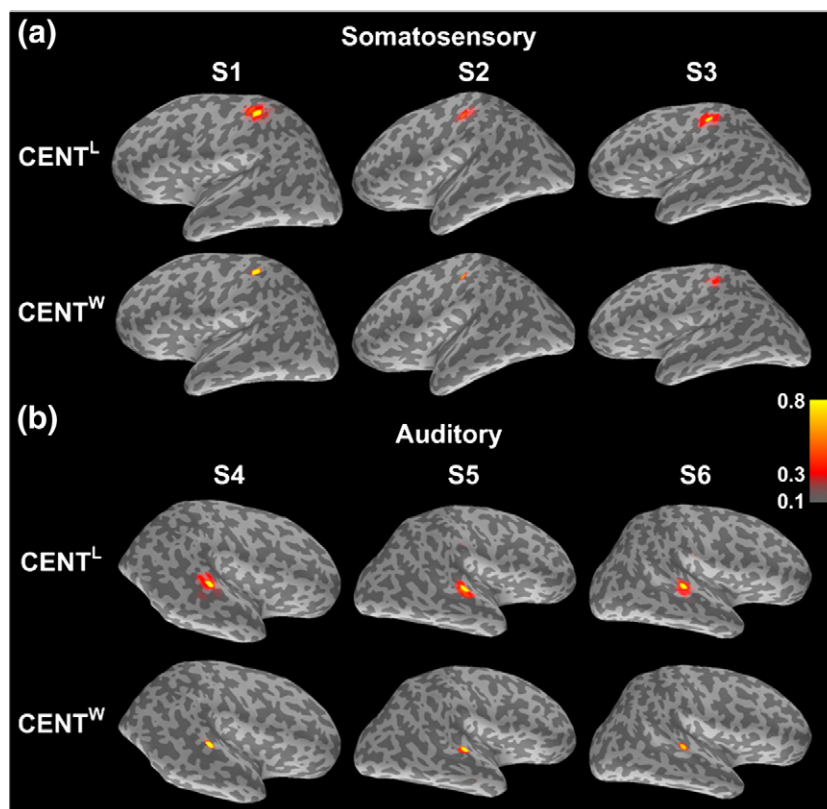


**Fig. 9.** (a) The reconstructed maps at 35 ms after stimulus onset for the somatosensory experiment. (b) The reconstructed maps around 70 ms after stimulus onset for the auditory experiment. S1 to S6 represent six different subjects. The activation strength is linearly scaled between 1 and 0 and is color-coded as illustrated by the color bar.

that the stimulus presented to one ear can evoke bilateral responses on primary auditory cortices at the superior temporal gyrus (Reite et al., 1982). SSI and MNE solutions revealed sources at not only the primary auditory cortex but also the middle temporal gyrus and the inferior parietal gyrus. These activation locations, to our knowledge, have not been reported in the literature. On the contrary,  $CENT^L$  and  $CENT^W$  detected prominent source on superior temporal gyrus in both hemispheres. Note that  $CENT^W$  can provide more focal source estimates than  $CENT^L$ , consistent with the simulation results (see Fig. 4).

To verify the stability of the CENT across subjects, we present maps of source estimates from the six subjects in the somatosensory and auditory MEG experiments. All frames in Fig. 9a were at 35 ms after the median nerve stimulus onset. The reconstructed sources in Fig. 9b were around 70 ms after the onset of auditory stimulus. For all subjects, the CENT can consistently detect contralateral SI activations and primary auditory cortex activation in the somatosensory and auditory experiments, respectively.

#### Method validation and sensitivity analysis

In all above simulations, we used the same source space to calculate the MEG forward and inverse solutions. This may give overly optimistic source localization performance (Kaipio and Somersalo, 2005). To examine the effect of this kind of an “inverse crime” (Kaipio

and Somersalo, 2005), we generated two forward solutions using either a dense source space with average 2.5 mm separation between sources or a coarse source space with average 10 mm separation between sources. Source estimates were calculated by using the coarse source space. Specifically, simulated sources were created with three different spatial extents (FWHM = 6, 18, and 36 mm) at three different locations (left SI, left SII and left inferior frontal cortex). The SNR of the measurement was set to 10. Source estimates using SSI, MNE,  $CENT^L$  and  $CENT^W$  were calculated separately, and the resulting estimates are shown in Fig. 10. We found that SSI gives better inverse estimates when using the coarse source space also for forward field calculations. On the contrary, MNE,  $CENT^L$  and  $CENT^W$  shows consistent source estimates regardless of the forward model being based either on a coarse or a dense source space. Furthermore,  $CENT^L$  and  $CENT^W$  give more accurate estimates for source location and spatial extent than MNE. Taken together, these results indicate that our proposed methods  $CENT^L$  and  $CENT^W$  are respectively viable options for more flexible distributed source modeling than what MNE (or SSI) can offer because stable estimates for sources of different spatial extent can be obtained from forward solutions with different source space densities.

Here we further investigated the sensitivity of CENT to different noises, parameter  $\alpha$ , and the orientation constraint parameter  $\theta$ . Simulations above used Gaussian noises. Here we tested CENT

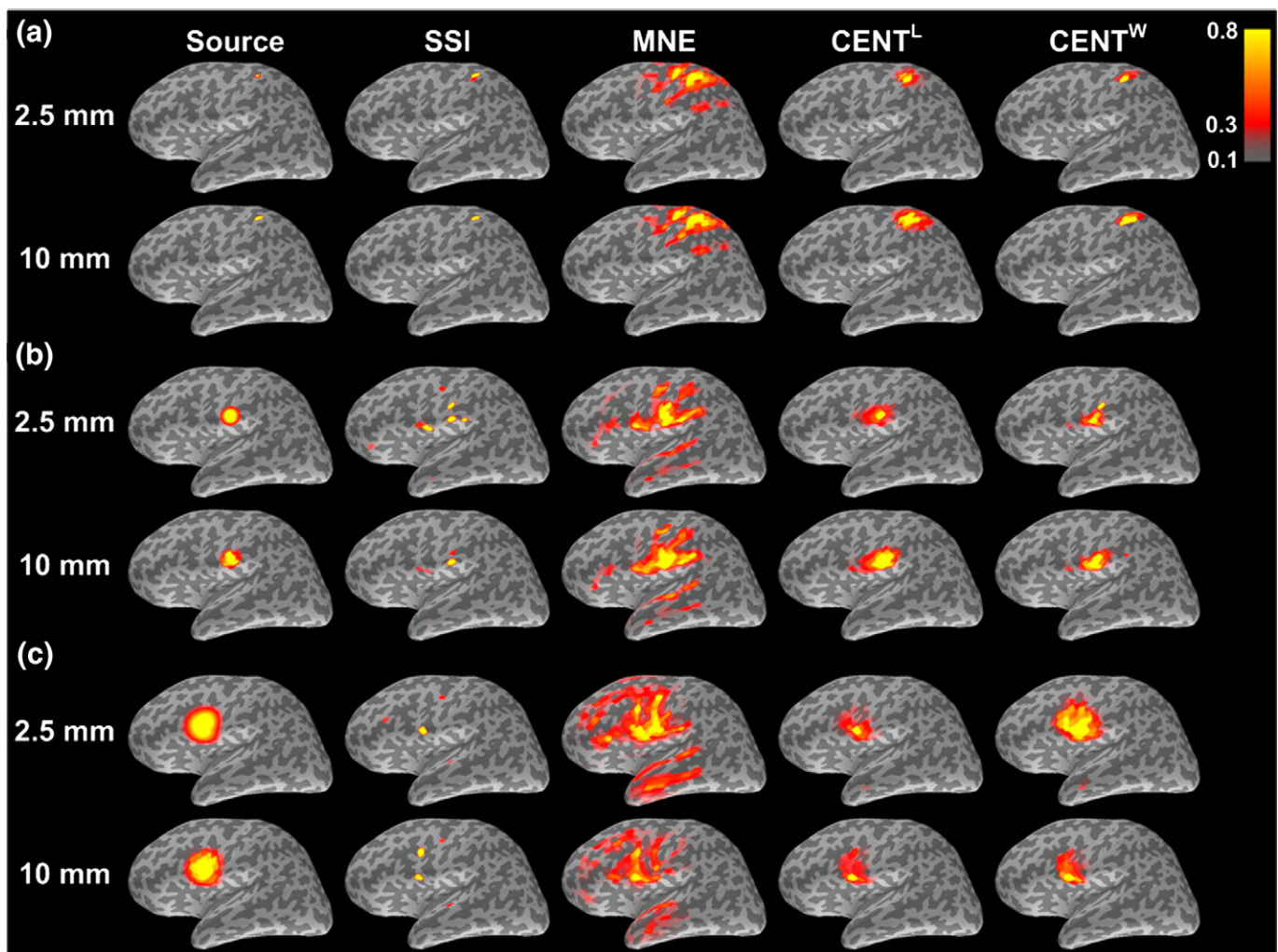


**Fig. 10.** The FWHMs of the simulated sources in panel (a), (b) and (c) are 6 mm, 18 mm, 36 mm respectively. The source estimates in the upper row of each panel were calculated from the MEG forward solution using a dense source space of average 2.5 mm between sources. The source estimates in the lower row of each panel were calculated from the MEG forward solution using a coarse source space of average 10 mm between sources. All sources were estimated using a coarse source space.

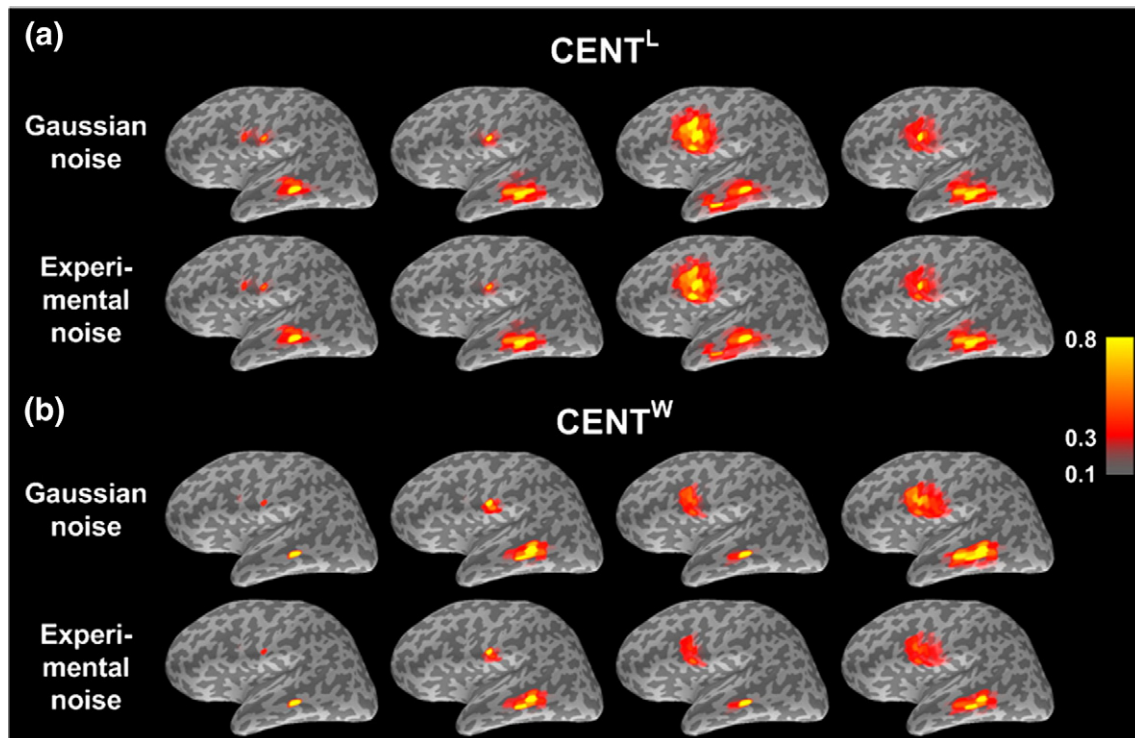


**Fig. 11.** Using the simulation source configurations shown in the top row in Fig. 4, the simulation results of  $CENT^L$  (in panel (a)) and  $CENT^W$  (in panel (b)) under additive Gaussian and experimental noise are demonstrated. The activation strength is linearly scaled between 1 and 0 and is color-coded as illustrated by the color bar.

performance using realistic noises derived from the pre-stimulus period. Using the simulation source configurations shown in the top row in Fig. 4, the simulation results of  $CENT^L$  and  $CENT^W$  under additive Gaussian and experimental noise are shown in Fig. 11. Simulations

of  $CENT^L$  or  $CENT^W$  using Gaussian and experimental noises gave marginal difference visually. This suggests that  $CENT$  is robust.

The parameter  $\alpha$  in this study was selected based on the simulations. To see how  $\alpha$  affects the performance in the analysis of

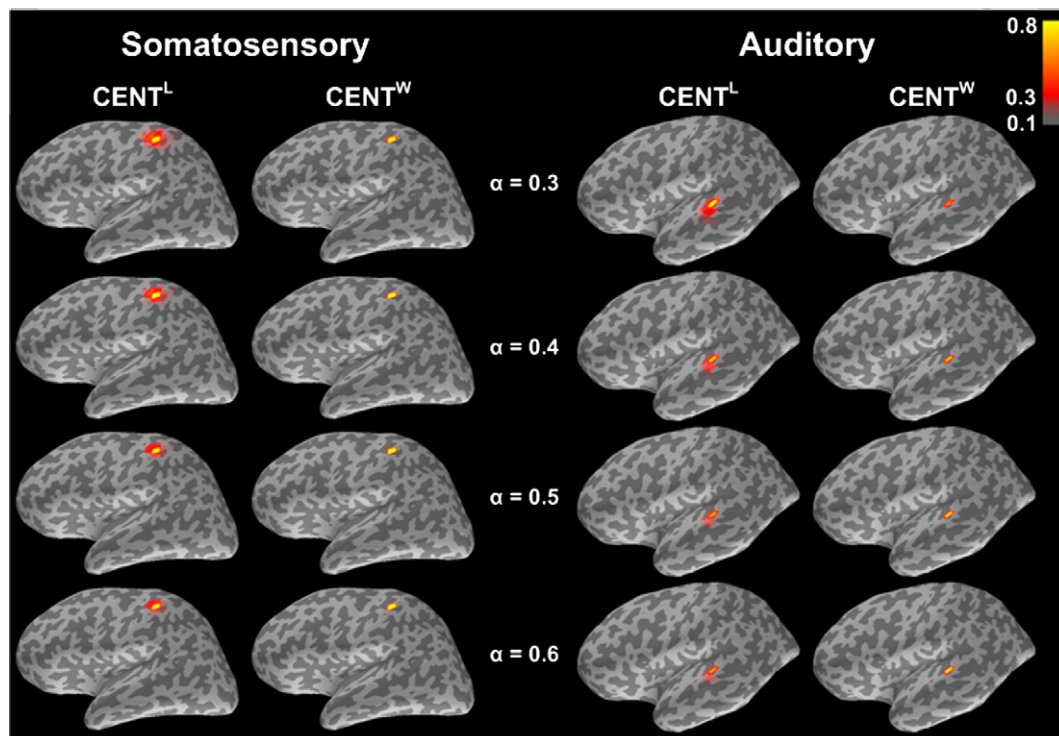


**Fig. 12.** The source estimates calculated from the somatosensory and auditory experimental data with  $\alpha$  varying between 0.3 and 0.6 are shown from the top to the bottom row, individually. The activation strength is linearly scaled between 1 and 0 and is color-coded as illustrated by the color bar.



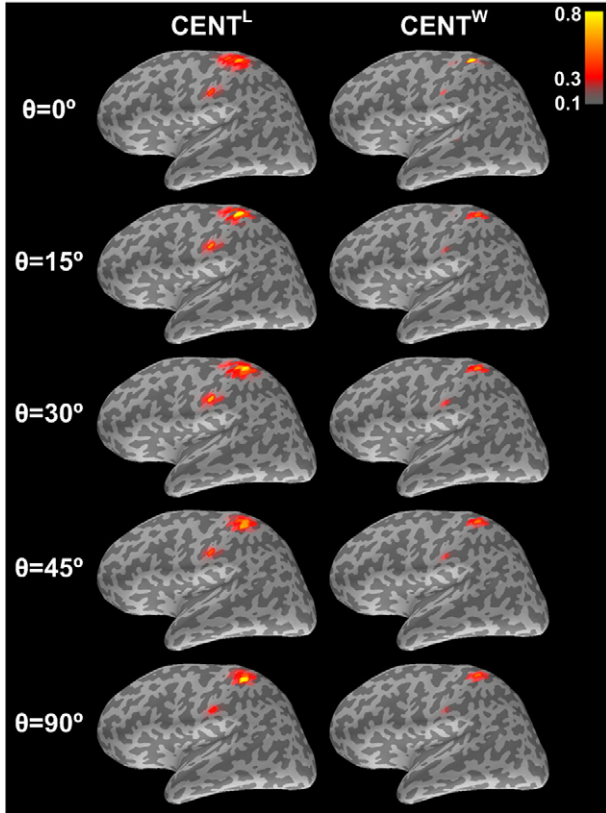


**Fig. 13.** The source estimates of  $CENT^L$  and  $CENT^W$  which were calculated from the somatosensory experimental data with the orientation parameter  $\theta_i = 0^\circ, 15^\circ, 30^\circ, 45^\circ$  and  $90^\circ$  are shown from the top to the bottom row, individually. The results are at the 82 ms after stimulus onset. The activation strength is linearly scaled between 1 and 0 and is color-coded as illustrated by the color bar.

*in vivo* data, we varied  $\alpha = 0.3 \sim 0.6$  parametrically for  $CENT^L$  and  $CENT^W$  to localize the responses of the somatosensory and auditory MEG data. Fig. 12 shows that no prominent changes of  $CENT^L$  and  $CENT^W$  were observed.  $CENT^L$  and  $CENT^W$  are not sensitive to  $\alpha$  varying between 0.3 and 0.6 in this data set.

The value of  $\theta_i$  controlled the orientation of current dipoles in Eq. (4).  $\theta_i$  was globally set to  $30^\circ$  in our study. Still, we tested the performance of  $CENT^L$  and  $CENT^W$  by different values of the parameter  $\theta_i$  using *in vivo* somatosensory data. Accordingly, we showed the localization of  $CENT^L$  and  $CENT^W$  using  $\theta_i = 0^\circ, 15^\circ, 30^\circ, 45^\circ$ , and  $90^\circ$ . Note that strict cortical orientation constraint corresponds to setting  $\theta_i$  to  $0^\circ$ , and the free cortical orientation constraint corresponds to setting  $\theta_i = 90^\circ$ . The results in Fig. 13 suggested that  $\theta_i$  varying between  $0^\circ$  and  $90^\circ$  can all detect SI and SII activations. However, our previous modeling study (Lin et al., 2006) suggested that more than 97% of the cortical patch has the standard deviation of the surface normal deviated from its average less than  $30^\circ$ . Therefore,  $\theta_i = 30^\circ$  can be a reasonable value for data analysis in practice.

## Discussion

In this paper we propose to incorporate compressibility as a constraint to solve the ill-posed MEG source localization problem. The proposed CENT method is a distributed source modeling technique. Our method is separated from other distributed source modeling methods by (1) the explicit quantification of the compressibility of source estimates by using a transformation matrix ( $M^L$  or  $M^W$ ), (2) the cost function can be tuned to obtain a balance between “transformed domain compressibility” and focal source characteristics (direct spatial compressibility), and (3) the constraint on the

consistency between measured and modeled data is flexibly bounded from above by a specified variance rather than constrained by a fixed residual variance (see Eq. (3)). The proposed objective function measures not only the  $\ell^1$ -norm of the source estimate globally, but also the transformed  $\ell^1$ -norm of the local  $\ell^2$ -norm of the dipole moments. The former prefers spatially focal source estimates, while the latter favors compressive source estimates in the transformed domain, which tends to be more spatially distributed when the transformation is the Laplacian matrix in comparison to the spherical wavelet transform. Taken together, both  $CENT^L$  and  $CENT^W$  can avoid explicit bias toward either focal or diffuse source estimates, as numerically validated in our simulations (Figs. 4 and 5). Since the cost function measures the  $\ell^2$ -norm of the orthogonal components in each source location, the cost is invariant for different current source orientations. The final source estimates can still be flexibly tuned such that they are predominantly perpendicular to the local cortical surface based on the realistic anatomical information from MRI. As demonstrated in our simulations and experimental results,  $CENT^L$  and  $CENT^W$  surpass sparse source imaging (SSI) (Ding and He, 2008) and the Minimum norm estimates (MNE) (Hamalainen and Ilmoniemi, 1984) by showing the capability of adaptively estimating the spatially focal and diffused sources (SD metric), a higher accuracy of source localization (DLE metric), and a higher detection power (ROC analysis) (see Fig. 5).

Laplacian matrix was previously introduced in the MEG/EEG inverse, such as LORETA (Pascual-Marqui et al., 1994), and FVR (Haufe et al., 2008). LORETA minimizes the  $\ell^2$ -norm of the Laplacian matrix transformed current sources to enforce the spatial smoothness. Thus LORETA generally prefers spatially smooth source estimates. Although FVR can balance between sparsity and smoothness of the estimated current sources, the solution is not as stable as  $CENT^L$ . This is because the constraint in FVR requires that the modeled measurement  $A_s(t)$  must match the given data  $Y_r(t)$ . Even with regularization, the FVR solution is more likely to be spatially unstable than  $CENT^L$  when the SNR is low (see Fig. 14). However, a strong bias toward a compressible solution can fail to match between the measurements and the predicted data. To balance between a sparse solution and the consistency, we defined  $\eta = \|A_s(t)\|_2 / \|Y_r(t) - A_s(t)\|_2$ , which evaluated the relative proportion between the size of the predicted measurement and the size of the residuals.  $\eta$  can also be regarded as a measure of SNR since the numerator and denominator respectively quantified the size of the predicted measurements and the residuals. In simulations, we expected that  $\eta$  calculated from the source estimates

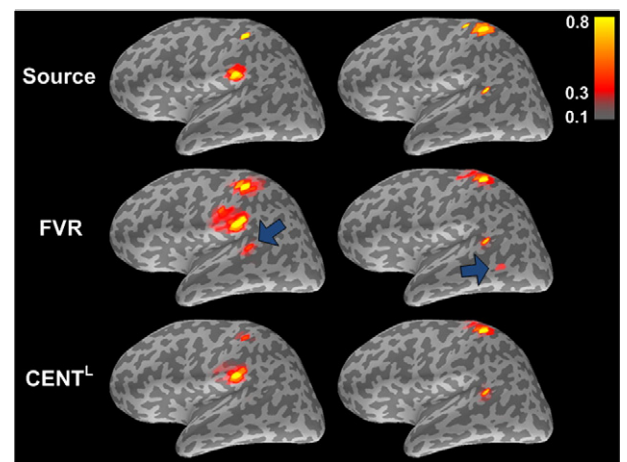


**Fig. 14.** Each column of the cortical maps represents simulated sources (top row) and the corresponding inverse solutions using FVR (middle row) and  $CENT^L$  (bottom row). The blue arrows indicate the false positive source estimates. The source estimates have been linearly scaled between 1 and 0 and were color-coded as illustrated by the color bar.

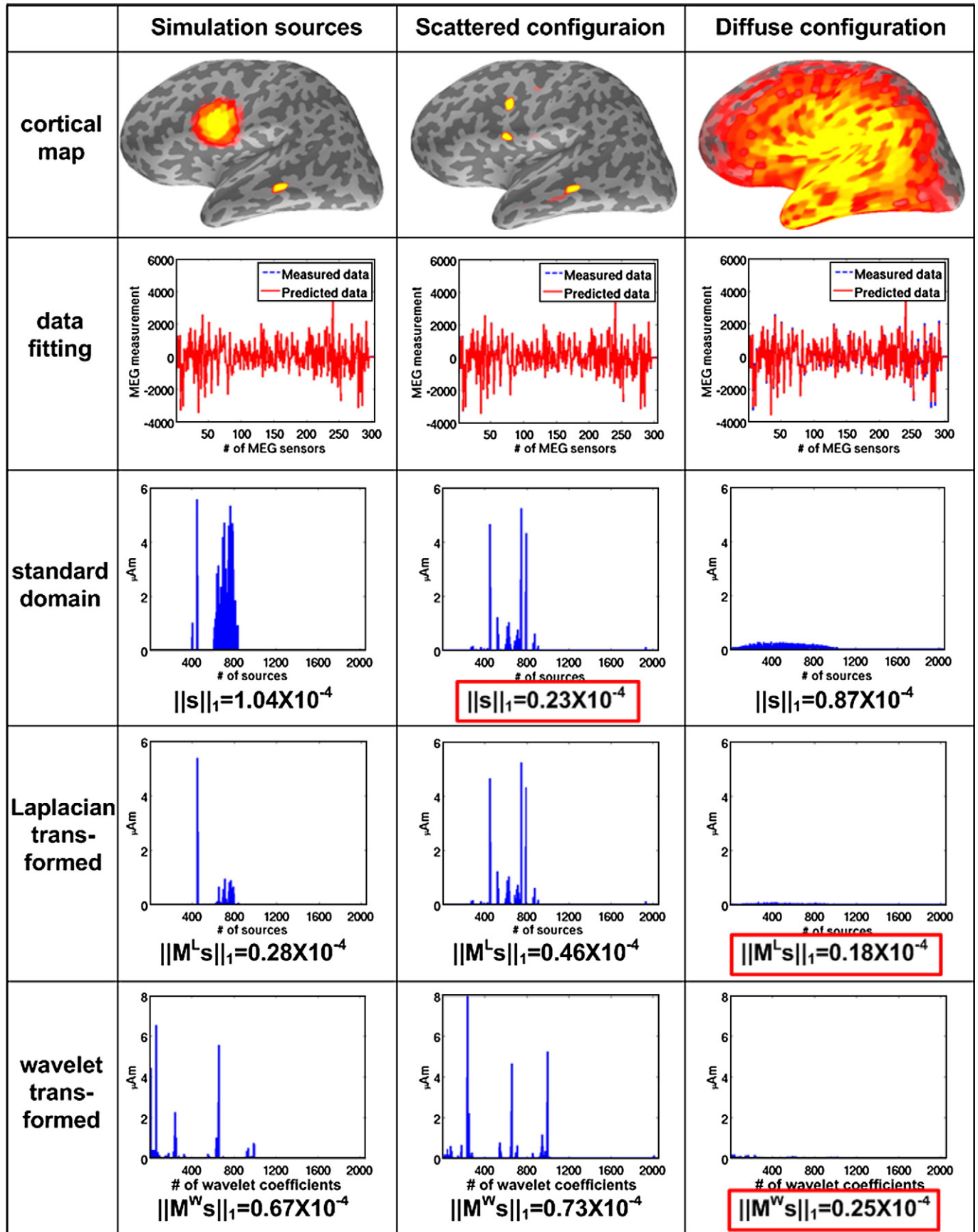


**Fig. 15.** The map of simulation sources is illustrated in the left column. Both the scattered source configuration (middle column) and the overly diffusive source configuration (right column) can generate measurements matched to the theoretical measurements from the simulation sources. From the third to the bottom rows are the source plots in either the standard domain or the transformed domain. The x axis represents the indices of sources and the y axis represents the source magnitude or the transformed coefficients. The red boxes highlight the maximum sparsity in either standard or transformed domain.

should approximate the specified SNR.  $\eta \leq \text{SNR}$  and  $\eta \geq \text{SNR}$ , respectively, indicates under-fitting and over-fitting. In our simulation,  $\text{CENT}^L$  had  $\eta = 1.6235 \pm 0.0831$  and FVR had  $\eta = 3.3799 \pm 0.1218$  when SNR was set to 2. This indicates that FVR over-fits the measurements and  $\text{CENT}^L$  under-fits the measurements with reasonable consistency.

Wavelet transform has been used in 2DII (Moran and Tepley, 2000) and MR-FOCUSS (Moran et al., 2005) for MEG/EEG source localization. The wavelet bases in 2DII or MR-FOCUSS depend on the measurement. This data-dependency renders both 2DII and MR-FOCUSS potentially sensitive to measurement noise. This problem can be partially corrected by restricting the degree of the freedom of the inverse problem using a rank-reduced forward solution. However, reconstructing the current source distribution using only a few spatial wavelet bases may yield inaccurate estimates. The  $\text{CENT}^W$  uses a complete wavelet basis set to tessellate the spatial distribution of current sources. Thus our method can avoid the inevitable trade-off between the solution stability and the accuracy of the spatial source distribution representation in 2DII or MR-FOCUSS. The noise sensitivity in the  $\text{CENT}^W$ , on the contrary, was mitigated by the adaptive control of the residual error (Eq. (5)) during the convex optimization.

The resolution of currently used source space can be too low to represent the curvature of the cortex accurately. To mitigate this challenge, we used the loose orientation constraint in the inverse modeling rather than in forward solution calculation. Previously it has been shown that the loose orientation constraint with a value of  $30^\circ$  can provide the optimal source localization to balance between the accurate cortical curvature and the stability of the localization (Lin et al., 2006).

The value of  $\alpha$  can be optimized using more sophisticated and computationally intensive methods. However,  $\text{CENT}^L$  and  $\text{CENT}^W$  have shown to perform successfully in analyzing empirical data using  $\alpha$  determined by our simulations. Independently, the residual variance  $\varepsilon$  being controlled in the specific way offers CENT the robustness toward noisy data in the  $\ell^1$ -norm minimization (Ding and He, 2008; Ou et al., 2009), as demonstrated in Fig. 14.

The CENT is closely related to other MEG/EEG inverse solvers. For example, replacing  $\mathbf{M}$  in Eq. (3) with an identity matrix  $\mathbf{I}$  and setting  $\theta_i$  to  $90^\circ$  for all  $i$  transforms the CENT to the SSI. Also, if we further set  $\varepsilon$  to zero and  $\theta_i$  to  $0^\circ$ , the solution of sparse distributed source modeling is virtually equal to that of MCE with strict orientation constraint. Moreover, FVR is also equivalent to the CENT approach when  $\mathbf{M} = \mathbf{M}^L$ ,  $\theta_i = 90^\circ$  and  $\varepsilon$  is set to zero. So in this sense CENT provides more general and flexible means for distributed source modeling by rendering these methods as special cases of the proposed approach.

Due to the ill-posed nature of the problem, estimating current sources across a fissure on a convoluted cortical surface is always challenging. In order to promote the spatial continuity of source estimates,  $\text{CENT}^L$  penalizes spatially separated sources across two banks of a sulcus. Thus  $\text{CENT}^L$  can avoid mislocalizing sources in such a scenario. Nevertheless,  $\text{CENT}^W$  can better distinguish separate but yet close-by sources than  $\text{CENT}^L$  (see Fig. 6). This advantage is a consequence of the topology of Butterfly wavelet basis (Fig. 2). Since many nodes in a basis are not immediate neighbors, the discontinuity between adjoining activated dipoles are less penalized in  $\text{CENT}^W$  than  $\text{CENT}^L$ . This wavelet-regularized discontinuity makes two spatially close sources distinguishable if the SNR of the data is sufficient.

## Conclusions

The proposed inverse technique CENT demonstrates the capability of reconstructing combinations of focal and diffuse current sources. Based on the hypothesis that current sources are also sparse after a spatial transformation, CENT recovers source estimates of high compressibility. This is achieved by simultaneously minimizing the  $\ell^1$ -norm of the spatially transformed sources and the  $\ell^1$ -norm of

current sources themselves. For instance, the Laplacian matrix ( $\text{CENT}^L$ ) and the spherical wavelets transform ( $\text{CENT}^W$ ) can be used as the spatial transformation, which yield somewhat different compressibility constraints. Compared to SSI and MNE, both  $\text{CENT}^L$  and  $\text{CENT}^W$  show superior source estimates with measurements arising from combined compact and extended current sources.  $\text{CENT}^L$  can avoid perplexing spatially separated source estimates across two banks of a sulcus and  $\text{CENT}^W$  makes spatially close yet not directly connected current sources more distinguishable. CENT is robust toward the noise because the residual error between the modeled data and the real measurement are adaptively controlled. The performance of CENT was quantitatively studied using simulations and *in vivo* somatosensory and auditory MEG data. We also demonstrated the reproducibility of CENT by showing consistency of the results across subjects. In conclusion, we consider the proposed CENT method to be a promising tool for adaptive modeling of neuronal current distributions underlying magnetic measurements of brain activity.

## Acknowledgments

We appreciate the technical supports by Chi-Che Chou at the Integrated Brain Research Unit in Veteran General Hospital, Taipei, Taiwan. We also thank Prof. Wen-Jui Kuo in Institute of Neuroscience in National Yang-Ming University for 3T MRI resource. This work was supported in part by the Department of Medical Imaging and 3T MRI Laboratory in National Taiwan University Hospital. Additionally, this work was supported by National Institutes of Health Grants by R01DA14178, R01HD040712, R01NS037462, P41 RR14075, R01EB006847, R01EB000790, R21EB007298, and the Mental Illness and Neuroscience Discovery Institute (MIND), NSC 97-2320-B-002-058-MY3 (National Science Council, Taiwan), NSC 97-2221-E-002-005 (National Science Council, Taiwan), and NHRI-EX98-9715EC (National Health Research Institute, Taiwan), Academy of Finland (127624), Finnish Cultural Foundation, and Finnish Foundation for Technology Promotion.

## Appendix A

Here we present the rationale of including the  $\|\mathbf{s}^{\prime 2}(t)\|_1$  term into the cost function of CENT. In preliminary analyses, we found that using only the compression constraint  $\|\mathbf{M}\mathbf{s}^{\prime 2}(t)\|_1$  might produce overly diffuse source estimates. This phenomenon is demonstrated in Fig. 15, which shows that either spatially highly diffuse (the right column of Fig. 15) or focal sources (the middle column of Fig. 15) can generate measurements matched to the theoretical measurements from the simulated sources (the left column of Fig. 15). We quantified the “sparsity” of all three source configurations by calculating the  $\ell^1$ -norm of the sources, Laplacian transformed sources, and wavelet transformed sources. Our results show that more sparse sources can be represented by a smaller  $\ell^1$ -norm value in the standard domain. We found that the true simulated source is approximately 4-fold less “sparse” ( $\|\mathbf{s}^{\prime 2}(t)\|_1 = 1.04 \times 10^{-4}$ ) than the discrete source estimates ( $\|\mathbf{s}^{\prime 2}(t)\|_1 = 0.23 \times 10^{-4}$ ). However, after either Laplacian or wavelet transformation, the true simulated source is also less sparse ( $\|\mathbf{M}^L\mathbf{s}^{\prime 2}(t)\|_1 = 0.28 \times 10^{-4}$  and  $\|\mathbf{M}^W\mathbf{s}^{\prime 2}(t)\|_1 = 0.67 \times 10^{-4}$ ) than the diffuse source estimates ( $\|\mathbf{M}^L\mathbf{s}^{\prime 2}(t)\|_1 = 0.18 \times 10^{-4}$  and  $\|\mathbf{M}^W\mathbf{s}^{\prime 2}(t)\|_1 = 0.25 \times 10^{-4}$ ). This indicates that constraining source estimates by maximizing either the sparsity of the source estimates or the sparsity of transformed source estimates alone can create a bias toward either spatially scattered or excessively diffuse source estimates, respectively. Thus we attempt to mitigate this challenge by combining the compressibility (the  $\ell^1$ -norm of the compression transformed source estimates) and the focality (the  $\ell^1$ -norm of the source estimates



themselves) constraints to obtain spatially sparse and contiguous source estimates.

## References

- Auranen, T., Nummenmaa, A., Hamalainen, M.S., Jaaskelainen, I.P., Lampinen, J., Vehtari, A., Sams, M., 2005. Bayesian analysis of the neuromagnetic inverse problem with l (p)-norm priors. *Neuroimage* 26, 870–884.
- Baillet, S., Riera, J.J., Marin, G., Mangin, J.F., Aubert, J., Garnero, L., 2001. Evaluation of inverse methods and head models for EEG source localization using a human skull phantom. *Phys. Med. Biol.* 46, 77–96.
- Boyd, S., 2004. *Convex Optimization*. Cambridge University Press.
- Bradshaw, L.A., Wikswo Jr., J.P., 2001. Spatial filter approach for evaluation of the surface Laplacian of the electroencephalogram and magnetoencephalogram. *Ann. Biomed. Eng.* 29, 202–213.
- Candes, E.J., Romberg, J., Tao, T., 2006. Robust uncertainty principles: exact signal reconstruction from highly incomplete frequency information. *IEEE Trans. Inf. Theory* 52, 489–509.
- Cottereau, B., Jerbi, K., Baillet, S., 2007. Multiresolution imaging of MEG cortical sources using an explicit piecewise model. *Neuroimage* 38, 439–451.
- Dale, A.M., Sereno, M.I., 1993. Improved Localization of Cortical Activity by Combining Eeg and Meg with Mri Cortical Surface Reconstruction - a Linear-Approach. *J. Cogn. Neurosci.* 5, 162–176.
- Dale, A.M., Fischl, B., Sereno, M.I., 1999. Cortical surface-based analysis. I. Segmentation and surface reconstruction. *Neuroimage* 9, 179–194.
- Ding, L., He, B., 2008. Sparse source imaging in electroencephalography with accurate field modeling. *Hum. Brain Mapp.* 29, 1053–1067.
- Donoho, D.L., 2006. Compressed sensing. *IEEE Trans. Inf. Theory* 52, 1289–1306.
- Engel, A.K., Konig, P., Gray, C.M., Singer, W., 1990. Stimulus-Dependent Neuronal Oscillations in Cat Visual Cortex: Inter-Columnar Interaction as Determined by Cross-Correlation Analysis. *Eur. J. Neurosci.* 2, 588–606.
- Fischl, B., Sereno, M.I., Dale, A.M., 1999. Cortical surface-based analysis. II: Inflation, flattening, and a surface-based coordinate system. *Neuroimage* 9, 195–207.
- Grant, M., Boyd, S., 2009. CVX. Stephen Boyd, p. Matlab software for disciplined convex programming (web page and software). <http://standford.edu/boyd/cvx>.
- Hamalainen, M., Ilmoniemi, R., 1984. Interpreting measured magnetic fields of the brain: estimates of current distributions. Helsinki University of Technology, Helsinki, Finland.
- Hamalainen, M.S., Sarvas, J., 1989. Realistic conductivity geometry model of the human head for interpretation of neuromagnetic data. *IEEE Trans. Biomed. Eng.* 36, 165–171.
- Hamalainen, M., Hari, R., Ilmoniemi, R.J., Knuutila, J., Lounasmaa, O.V., 1993. Magnetoencephalography - Theory, Instrumentation, and Applications to Noninvasive Studies of the Working Human Brain. *Rev. Mod. Phys.* 65, 413–497.
- Hari, R., Forss, N., 1999. Magnetoencephalography in the study of human somatosensory cortical processing. *Philos. Trans. R. Soc. Lond. B Biol. Sci.* 354, 1145–1154.
- Haufe, S., Nikulin, V.V., Ziehe, A., Muller, K.R., Nolte, G., 2008. Combining sparsity and rotational invariance in EEG/MEG source reconstruction. *Neuroimage* 42, 726–738.
- Helmholtz, H., 1853. Ueber einige Gesetze der Vertheilung elektrischer Ströme in körperlichen Leitern, mit Anwendung auf die thierisch-elektrischen Versuche. *Ann. Phys. Chem.* 89 (211–233), 353–377.
- Huang, M.X., Dale, A.M., Song, T., Halgren, E., Harrington, D.L., Podgorny, I., Canive, J.M., Lewis, S., Lee, R.R., 2006. Vector-based spatial-temporal minimum L1-norm solution for MEG. *Neuroimage* 31, 1025–1037.
- Kaipio, J., Somersalo, E., 2005. *Statistical and computational inverse problems*. Springer, New York.
- Limpiti, T., Van Veen, B.D., Wakai, R.T., 2006. Cortical patch basis model for spatially extended neural activity. *IEEE Trans. Biomed. Eng.* 53, 1740–1754.
- Lin, F.H., Belliveau, J.W., Dale, A.M., Hamalainen, M.S., 2006. Distributed current estimates using cortical orientation constraints. *Hum. Brain Mapp.* 27, 1–13.
- Lustig, M., Donoho, D., Pauly, J.M., 2007. Sparse MRI: The application of compressed sensing for rapid MR imaging. *Magn. Reson. Med.* 58, 1182–1195.
- Matsuura, K., Okabe, Y., 1995. Selective minimum-norm solution of the biomagnetic inverse problem. *IEEE Trans. Biomed. Eng.* 42, 608–615.
- Mesulam, M.-M., 1990. Large-scale neurocognitive networks and distributed processing for attention, language, and memory. *Ann. Neurol.* 28, 597–613.
- Molins, A., Stufflebeam, S.M., Brown, E.N., Hamalainen, M.S., 2008. Quantification of the benefit from integrating MEG and EEG data in minimum l2-norm estimation. *Neuroimage* 42, 1069–1077.
- Moran, J.E., Tepley, N., 2000. Two dimensional inverse imaging (2DII) of current sources in magnetoencephalography. *Brain Topogr.* 12, 201–217.
- Moran, J.E., Bowyer, S.M., Tepley, N., 2005. Multi-Resolution FOCUSS: a source imaging technique applied to MEG data. *Brain Topogr.* 18, 1–17.
- Mosher, J.C., Lewis, P.S., Leahy, R.M., 1992. Multiple dipole modeling and localization from spatio-temporal MEG data. *IEEE Trans. Biomed. Eng.* 39, 541–557.
- Nakata, K., Yamashita, M., Fujisawa, K., Kojima, M., 2006. A parallel primal-dual interior-point method for semidefinite programs using positive definite matrix completion. *Parallel Comput.* 32, 24–43.
- Okada, Y.C., Wu, J., Kyuhou, S., 1997. Genesis of MEG signals in a mammalian CNS structure. *Electroencephalogr. Clin. Neurophysiol.* 103, 474–485.
- Oostendorp, T.F., van Oosterom, A., 1989. Source parameter estimation in inhomogeneous volume conductors of arbitrary shape. *IEEE Trans. Biomed. Eng.* 36, 382–391.
- Ou, W., Hamalainen, M.S., Golland, P., 2009. A distributed spatio-temporal EEG/MEG inverse solver. *Neuroimage* 44, 932–946.
- Pascual-Marqui, R.D., Michel, C.M., Lehmann, D., 1994. Low resolution electromagnetic tomography: a new method for localizing electrical activity in the brain. *Int. J. Psychophysiol.* 18, 49–65.
- Peyre, G., 2008. *Toolbox Wavelets on Meshes* <http://www.mathworks.com/matlabcentral/fileexchange/17577>. Paris.
- Reite, M., Zimmerman, J.T., Zimmerman, J.E., 1982. MEG and EEG auditory responses to tone, click and white noise stimuli. *Electroencephalogr. Clin. Neurophysiol.* 53, 643–651.
- Schroder, P., Sweldens, W., 1995. SphericalWavelets: Efficiently Representing Functions on the Sphere. *Computer Graphics (SIGGRAPH '95 Proceedings)*, pp. 161–172.
- Shannon, C.E., 1948. A Mathematical Theory of Communication. *Bell Syst. Tech. J.* 27, 379–423.
- Silva, L.R., Amitai, Y., Connors, B.W., 1991. Intrinsic oscillations of neocortex generated by layer 5 pyramidal neurons. *Science* 251, 432–435.
- Taubman, D.S., Marcellin, M.W., 2002. *JPEG2000: image compression fundamentals, standards, and practice*. Kluwer Academic Publishers, Boston.
- Uutela, K., Hamalainen, M., Somersalo, E., 1999. Visualization of magnetoencephalographic data using minimum current estimates. *Neuroimage* 10, 173–180.
- Van Trees, H.L., 1968. *Detection, estimation, and modulation theory*. Wiley, New York.
- Wood, Z.J., Schroder, P., Breen, D., Desbrun, M., 2000. Semi-regular mesh extraction from volumes. *Proceedings of the conference on Visualization*, Salt Lake City, Utah, United States, pp. 275–282.